



The use of digital image correlation in the biomechanical area: a review

Marco Palanca, Gianluca Tozzi & Luca Cristofolini

To cite this article: Marco Palanca, Gianluca Tozzi & Luca Cristofolini (2016) The use of digital image correlation in the biomechanical area: a review, International Biomechanics, 3:1, 1-21, DOI: [10.1080/23335432.2015.1117395](https://doi.org/10.1080/23335432.2015.1117395)

To link to this article: <http://dx.doi.org/10.1080/23335432.2015.1117395>



© 2015 The Author(s). Published by Taylor & Francis



Published online: 21 Dec 2016.



Submit your article to this journal [↗](#)



View related articles [↗](#)



View Crossmark data [↗](#)

The use of digital image correlation in the biomechanical area: a review

Marco Palanca^a , Gianluca Tozzi^b and Luca Cristofolini^c 

^aSchool of Engineering and Architecture, University of Bologna, Bologna, Italy; ^bSchool of Engineering, University of Portsmouth, Portsmouth, UK; ^cSchool of Engineering and Architecture, Department of Industrial Engineering, University of Bologna, Bologna, Italy

ABSTRACT

This paper offers an overview of the potentialities and limitations of digital image correlation (DIC) as a technique for measuring displacements and strain in biomechanical applications. This review is mainly intended for biomechanists who are not yet familiar with DIC. This review includes over 150 papers and covers different dimensional scales, from the microscopic level (tissue level) up to macroscopic one (organ level). As DIC involves a high degree of computation, and of operator-dependent decisions, reliability of displacement and strain measurements by means of DIC cannot be taken for granted. Methodological problems and existing solutions are summarized and compared, whilst open issues are addressed. Topics addressed include: preparation methods for the speckle pattern on different tissues; software settings; systematic and random error associated with DIC measurement. Applications to hard and soft tissues at different dimensional scales are described and analyzed in terms of strengths and limitations. The potentialities and limitations of DIC are highlighted, also in comparison with other experimental techniques (strain gauges, other optical techniques, digital volume correlation) and numerical methods (finite element analysis), where synergies and complementarities are discussed. In order to provide an overview accessible to different scientists working in the field of biomechanics, this paper intentionally does not report details of the algorithms and codes used in the different studies.

ARTICLE HISTORY

Received 29 December 2014
Accepted 3 November 2015

KEYWORDS

Digital image correlation (DIC); *in vitro* biomechanical tests; displacement and strain measurement; accuracy and precision error; hard tissue; soft tissue

1. Introduction

1.1. Why is it important to measure full-field displacements and strains?

The measurement of displacement and strain is an important task in experimental biomechanics because it allows the characterization of biological tissues, organs and their interactions with biomedical devices. For instance, the stiffness is computed as the ratio between the load and the displacement; bone remodelling is a well-known stress/strain-driven process (Wolff's law); bone fracture is governed by a strain-based failure criterion (Bayraktar et al. 2004). Due to the features of biological specimens, which are mainly inhomogeneous and anisotropic, it is extremely important to obtain full-field measurements, ideally with a contactless technique (Haddadi & Belhabib 2008). On the computational side, finite element (FE) analysis results require experimental data as an input, and must be validated against experimental tests. Pointwise measurements, such as the ones provided by strain gauges, sometimes are not sufficient to fully monitor an experiment. Full-field measurements are very important when local damages, such as a crack initiation or propagation, must be identified.

1.2. Overview of full-field, contactless optical measurement techniques

Among the different optical techniques, the ones most frequently used nowadays are the digital ones that allow automation of the acquisition and analysis process. After an initial stage of general diffidence during the 80s followed by the first successful applications on mechanical tests in the 90s, optical measurement techniques become very appealing and are increasingly applied in the industrial and research environments. These measurement techniques allow:

- Full-field measurement through visualization of strain gradients and concentrations. This produces a more complete description of the behaviour of biological specimens during *in vitro* tests;
- Contactless measurements that enable the measurement of strain without disturbing the local mechanical response of the material. This requirement is particularly important for deformable materials such as soft tissues (liver, intervertebral discs, etc.);
- Relatively simple preparation of the surface compared to other measurement techniques, such

CONTACT Luca Cristofolini  luca.cristofolini@unibo.it

© 2015 The Author(s) Published by Taylor & Francis.

This is an Open Access article distributed under the terms of the Creative Commons Attribution License (<http://creativecommons.org/licenses/by/4.0/>), which permits unrestricted use, distribution, and reproduction in any medium, provided the original work is properly cited.

as the application of strain gauges or fibre Bragg grating sensors.

Such features are mandatory for typical biomechanical tests on non-homogeneous and anisotropic materials, and specimens with a complex geometry. At the same time, an optical measurement technique must be accurate and precise.

Some optical measurement techniques, such as holographic interferometry, speckle interferometry (including its digital version, electronic speckle pattern interferometry) are highly accurate, but they are too sensitive to small displacements, and therefore unsuitable for deformable materials such as biological tissues (Freddi et al. 2015). Other optical techniques, such as Moiré interferometry, require the preparation of a regular pattern on the specimen surface (Post & Han 2008; Freddi et al. 2015), which can be very difficult for biological specimens having an irregular geometry. In general, all such techniques have recently found very limited application because of their complexity in practical use. A promising optical technique for the biomechanical field is the digital image correlation (DIC) (Sutton et al. 2009), which is able to overcome most such limitations (Freddi et al. 2015).

1.3. Aim

The purpose of this paper is to provide an overview on the operating principles of DIC, and of its applications in biomechanical area. This review is conceived for biomechanists who want to improve their knowledge about DIC, and need to critically understand the underlying benefits and limitations related to biomechanical applications.

2. Introducing DIC

2.1. History of DIC

The increasing diffusion of DIC can be explained by its flexibility, scalability to a wide range of dimensions, the robustness of its operating principle, and its (apparent) ease of use (Tyson et al. 2002; Pan et al. 2009; Sutton et al. 2009; Soons et al. 2012; Amiot et al. 2013; Freddi et al. 2015). DIC was introduced in the early of 80s, with the first system developed at the University of South Carolina (Peters & Ranson 1982; Sutton et al. 1983; Chu et al. 1985; Bruck et al. 1989), and has been subsequently improved (Luo et al. 1992, 1994; Helm et al. 1996). The first applications of DIC in biomechanics date back to the 90s (Bay 1995; Bay, Yerby et al. 1999). During the first decade of the new century, DIC was applied regularly in the biomechanical field, with home-written algorithms (Nicoletta et al. 2001; Zhang et al. 2002a, 2002b). Later on, several companies developed proprietary DIC systems (Tables 1–2). Additionally, DIC

libraries are also available as part of software suites, such as MATLAB (MathWorks, Natick, MA, USA) and Mathematica (Wolfram, Champaign, IL, USA). Reviews on the use of DIC for traditional engineering materials can be found (Hild & Roux 2006; Pan et al. 2009).

2.2. Operating principle

DIC is based on sets of images of the surface of the specimen in the undeformed (reference) and deformed states (Figure 1). DIC can be implemented both in a bi-dimensional (2D-DIC, with a single camera) and a tri-dimensional (3D-DIC, using two or more cameras) version. A calibration is necessary to initialize the spatial correlation processes of DIC. The images are divided in smaller sub-images (facets), and a matching algorithm is used to match the facets between the reference and deformed states. The displacement field is then computed. Subsequently, the strain field is obtained by derivation. More details about the operating principle are reported in Appendix 1. The main advantages and disadvantages of DIC (Schmidt et al. 2003; Sutton et al. 2009) are summarized in Table 3.

3. Surface pattern preparation on biological specimens

For an optimal use of DIC, the surface of interest must have a random pattern, which deforms together with the specimen surface. If the specimen presents a natural random pattern, due to an intrinsic texture or inhomogeneity, this can be directly exploited by the DIC system. In all other cases, a random pattern must be generated. To ensure accuracy and precision of the computed displacements and strains, the speckle pattern should meet some requirements (Lecompte et al. 2006; Yaofeng & Pang 2007; Pan et al. 2008; Sutton et al. 2009; Barranger et al. 2010; Crammond et al. 2013):

- Random distribution, in order to make each area of the surface of the specimen univocally identifiable;
- High contrast, to allow the image correlation algorithm works effectively;
- Black/white ratio of 50:50, to avoid regions that cannot be properly recognized;
- Roughness should be kept at minimum, in order to avoid alteration of the surface geometry.
- Probably the most important issue in biomechanical applications is the size of the speckle dots (in relation to the specimen size), in order to optimally exploit the resolution of the camera (Lionello & Cristofolini 2014). In fact, the larger the measurement window, the larger the corresponding area

covered by each pixel (for a given sensor resolution) and therefore the dots of the speckle pattern. In order to obtain the best speckle pattern for the specific application, the dimension of the speckle should be different for each application. The ideal size of the speckle dots corresponds to 3–5 pixels (Sutton et al. 2009). The magnification factor, M , is defined as the ratio between the number of pixels on the long side of the camera sensor and the long side of the measurement window (M indicates how many pixels correspond to the unit length of the physical specimen). Thus, the ideal size of the speckle dots corresponds to 3–5 pixels divided by M . For example, using a camera-sensor of 5 Megapixels (2448×2050 pixels) on a field of view of $2 \text{ mm} \times 2 \text{ mm}$ (e.g. few trabeculae), yields an optimal dimension of the speckle pattern of about 0.003 mm . The same camera-sensor applied to a larger area of interest of $2 \text{ m} \times 2 \text{ m}$ (e.g. a whole human body) would require larger speckle dots, about 3.25 mm .

Recently, a tool (a script in MATLAB) was developed to evaluate the quality and suitability of a given speckle pattern for a given DIC application (Estrada & Franck 2015).

The techniques to prepare a speckle pattern most commonly used are (Tables 1–2):

- High-contrast paint sprayed with an airbrush air-gun (Figure 2(a)): this technique is suitable for both small and large deformations (Barranger et al. 2010; Lionello & Cristofolini 2014), as the speckle dot itself is strained during the deformation.
- A dispersion of toner/graphite powder (Figure 2(b)) randomly placed on the specimen: this is a remarkable technique in case of small deformations, particularly for soft tissues, due to an optimal adhesion on moist surfaces. Conversely, in case of large deformations it can produce an underestimation of the strain, as the powder particles displace but do not strain when the underlying specimen is deformed (Barranger et al. 2010).

The black-on-white speckle pattern is most frequently used: first a uniform white background is created, on which black speckles are added. This preparation provides the optimal contrast. If the surface of the specimen itself is already of a light colour (i.e. bone), preparation of the white background could be avoided. The use of water-based paints minimizes the alteration on biological specimens (Freddi et al. 2015).

In sporadic cases (Genovese, Lee et al. 2013, Lionello et al. 2014; Luyckx et al. 2014), especially for soft tissues, the white-on-black speckle pattern can be used (Figure

2(c)). The difference lies in the colour of the background (black or dark blue), and of the speckles (white). The dark background is obtained through immersion of the specimen in some colouring agent (typically methylene blue staining). This prevents delamination and crumbling of the background layer even at large deformations, which may occur with a paint layer. The white speckle pattern is then produced with an airgun. It has been shown that application of methylene blue on ligaments increases their stiffness by 0.8%. Deposition of the white pattern further increased the stiffness to 1.7% (Lionello et al. 2014).

A different preparation of the specimen was used, where ethidium bromide nuclear staining was used to incorporate a high-contrast pattern (Ning et al. 2010). This allows a permanent incorporation of the pattern into the microstructure of the specimen.

4. Correlation algorithm parameters

In order to obtain the best results from this versatile measurement technique, a number of parameters must be adapted to the specific application (Figure 3):

- Facet size (dimension of the sub-image used in the computation);
- Grid spacing (step between consecutive facets);
- Strain computation window (typically larger than the single facet) used to derive the strain field over a larger area, in order to attenuate the noise
- Validity quote (Minimum percentage of computation points that must be available for strain to be calculated over a given computation window);
- Filtering (sometimes applied at the different stages of the correlation to reduce noise).

The values assigned to such parameters determine the accuracy, precision and spatial resolution (Palanca, Brugo et al. 2015; see below). There is no universally optimal set of parameters, due to the numerous possible uses of DIC, particularly in biomechanics. A choice must be made in relation to the specific application (i.e. tissue, anatomy and dimensions of the specimens). Only in few papers the DIC parameters are detailed (Tables 1–2).

4.1. Facet size

The digital images are divided into sub-images, called facets, of $M \times N$ pixels (typically squared). Each facet is represented by a grey-level distribution, which is, in most cases, interpolated by a bi-cubic spline to obtain an approximation of grey-scale between adjacent pixels. Each facet is summarized by the information about the pattern, and its location in space. The correlation algorithm identifies the best-matching region at different load steps. The influence

Table 1. Papers presenting applications of DIC to biomechanical investigations of the soft tissues.

Specimen	Field of view	Pixel size (μm)	Type of random pattern	Type of mechanical test	Reported quantities	Number of specimens	DIC system	DIC parameters	Note	References
<i>Cardiovascular – human</i>										
Human aortic tissue	N.A.	N.A.	N.A.	Inflation test	Displacement and strain distribution	4	Aramis 3D	N.A.		Kim et al. (2011)
Human heart	100 mm \times 100 mm	147	Natural pattern	Myocardial movements	Displacement and strain distribution	1	DaVis	F_S: 121 \times 121; G_S: 1	<i>In vivo</i>	Hokka et al. (2015)
<i>Cardiovascular – animal</i>										
Bovine aorta	25 mm \times 18 mm	20	Airbrush	Tensile test	Full-field displacement; strain distribution	N.A.	Home written	N.A.		Zhang et al. (2002a)
Mice carotid arterial	290 μm \times 770 μm	2.2	Powder	Pressure test	Lagrangian strain	1	Vic-3D modified	F_S: 43 \times 43; G_S: 5		Sutton, Ke et al. (2008)
Mice carotid arterial	N.A.	N.A.	Ethidium bromide nuclear	Pressure and tensile test	Displacement and strain distribution	1	Vic-3D	F_S: 15 \times 15	Singular speckle pattern	Ning et al. (2010)
Mice carotid arteries	N.A.	N.A.	Airbrush	Pressure test	Strain distribution	1	Home written	G_S: 8 \times 4		Genovese, Lee et al. (2011)
Mice suprarenal aorta with abdominal aneurysm	N.A.	N.A.	Airbrush	Pressure test on lesions	Strain distribution	1	Home written	N.A.	pDIC	Genovese et al. (2012)
Mice suprarenal aorta	N.A.	N.A.	Airbrush	Pressure test	Strain distribution	1	Home written	N.A.		Genovese, Lee et al. (2013)
Porcine aortic arch	N.A.	N.A.	Airbrush	Pressure test	Strain distribution	1	Home written	N.A.	pDIC	Genovese and Humphrey (2015)
Porcine left ventricular wall	N.A.	N.A.	Airbrush	Indentation test	Displacement and strain distribution	1	Home written	N.A.	Combined with a fringe projection method	Genovese et al. (2015)
<i>Cartilage – human</i>										
Human cartilage from patellae	N.A.	4	N.A.	Tensile test	Normal strain	10	Home written	N.A.		Narmoneva (2002)
<i>Cartilage – animal</i>										
Bovine carpo-metacarpal joint cartilage	888 μm \times 703 μm	0.683	Natural pattern	Unconfined compression	Young's modulus; Poisson ratio	21	N.A.	F_S: 20/40/60; G_S: from 8 to 120		Wang et al. (2002)
Bovine articular cartilage	N.A.	N.A.	N.A.	Unconfined compression	Young's modulus; Poisson ratio	15	Home written	N.A.		Wang et al. (2003)
Porcine articular cartilage	N.A.	59.56	Airbrush	Tensile test	Displacement distribution	1	Home written	N.A.	Comparison with ESPI	Zhang et al. (2005)
Porcine intervertebral disc (FSU L4-L5)	51.2 mm \times 10.2 mm	23	Powder	Compression test	Strain distribution	1	Home written	F_S: 9 \times 9		Spera et al. (2011)

Table 1. (Continued)

Specimen	Field of view	Pixel size (μm)	Type of random pattern	Type of mechanical test	Reported quantities	Number of specimens	DIC system	DIC parameters	Note	References
Chondrocyte-seeded agarose hydrogels	N.A.	N.A.	Natural pattern	Compression test	Axial and lateral strain	N.A.	Home written	N.A.		Kelly et al. (2006)
Beaks of granivorous birds	14 mm \times 17 mm	6.8	Airbrush	Bending test	Displacement distribution; in-plane normal strain, in-plane shear strain	2	Home written	F_S: 21 \times 21; G_S: 10; C_W: 50 \times 50		Soons et al. (2012)
Scales from <i>Cyprinus carpio</i>	5.6 mm \times 4.2 mm	4	Airbrush	Tensile test	Strain distribution	10	Home written	N.A.	Microscopy DIC	Marino Cugno Garrano et al. (2012)
Mice skin	N.A.	N.A.	N.A.	Tensile test	Strain distribution	6	N.A.	N.A.		Karimi et al. (2015)
<i>Internal organs – human</i>										
Human cervical tissue	N.A.	N.A.	Airbrush	Tensile test	Axial and lateral strain	10	Vic-2D	N.A.		Myers et al. (2008)
Human liver	25 mm \times 25 mm		Airbrush	Inflation test	Displacement and strain distribution	15	Vic-3D	F_S: 21 \times 21; G_S: 5		Brunon et al. (2011)
<i>Internal organs – animal</i>										
Porcine liver	100 mm \times 80 mm	3.3	Airbrush	Indentation test	Deformation distribution	1	Aramis 3D	N.A.		Ahn and Kim (2010)
Porcine livers	N.A.	N.A.	Natural pattern	Tensile test	Strain in longitudinal direction	10	Home written	N.A.		Gao and Desai (2010)
Porcine brain	N.A.	N.A.	Airbrush	Unconfined compression test	Displacement distribution	N.A.	Vic-3D	N.A.		Libertiaux et al. (2011)
Lamb gallbladder	N.A.	N.A.	Airbrush	Pressure test	Full-strain distribution	1	Home written	F_S: 21 \times 21; C_W: 41 \times 41 px	pDIC	Genovese et al. (2014)
Human lower limb muscles	N.A.	N.A.	Natural pattern	Compression test	Displacement distribution	4	Home written	N.A.	Use of ultrasound images	Affagard et al. (2014)
<i>Artificial soft tissue</i>										
Heart valve tissue	N.A.	N.A.	N.A.	Indentation test	Displacement and strain distribution	N.A.	Aramis 3D	N.A.		Cox et al. (2008)
Synthetic vocal fold	N.A.	11	Airbrush	Airflow test	Displacement and strain distribution	N.A.	Vic-3D	F_S: 23 \times 23	Use of high speed camera; 3D with a single camera	Spencer et al. (2008)
Silicon gel	N.A.	N.A.	Painted	Indentation test	Deformation distribution	1	Vic-3D	N.A.		Moerman et al. (2009)

Notes: References are listed in chronological order within each subsection.

N.A = information not available.

F_S = facet size.

G_S = grid spacing.

C_W = computation window.

Istra-4D by Dantec Dynamics (Skovlunde, Denmark), Aramis 3D by GOM (Braunschweig, Germany), Vic-2D and Vic-3D by Vision Solution (Irvine, California, USA), StrainMaster and DaVis by LaVision (Goettingen, Germany), ProAnalyst by Xcited (Woburn, Maine, USA).

Rapid Correlation by XStream Software (Ottawa, Ontario, Canada).

Table 2. Papers presenting applications of DIC to biomechanical investigations of hard tissue.

Specimen	Field of view	Pixel size (μm)	Type of random pattern	Type of mechanical test	Reported quantities	Number of specimens	DIC system	DIC parameters	Note	References
<i>Tissue level – human</i>										
Trabecular bone from human femoral head	N.A.	N.A.	Natural pattern	Compression test	Displacement distribution	6	Home written			Bay (1995)
Slices of human thoracic spinal motion segments	N.A.	N.A.	Natural pattern	Compression test	Strain distribution	6	Home written		With radiographs unit	Bay, Yerby et al. (1999)
Trabecular bone of human cadaveric knee	N.A.	N.A.	Natural pattern	Compression test	Strain distribution; principal strain	8	Home written		With radiographs unit	McKinley and Bay (2003)
Interface human bone cement	N.A.	8.9	N.A.	Shear fatigue test	Interface displacement	25	Rapid Correlation	F_S: 40 × 40		Mann et al. (2008)
Human trabecular bone from femur	N.A.	N.A.	Airbrush	Compression test	Displacement and strain distribution	12	Istra-4D	N.A.		Cyganik et al. (2014)
Human cortical bone from femur	3.6 mm ² × 2.7 mm ²	2.6	Natural pattern	Shear test	Displacement and strain distribution	29	DaVis		Use of optical microscope	Tang et al. (2015)
<i>Tissue level – animal</i>										
Cortical bone of bovine tibias	180 μm^2 × 141 μm^2 ; 445 μm^2 × 350 μm^2	0.137; 0.339	Natural pattern	Micro-crack in stressed cortical bone	Principal strain	N.A.	Home written	F_S: 9 × 9 × 19 × 19; 31 × 31; 63 × 63		Nicoletta et al. (2001)
Cortical bone of bovine tibias	180 μm^2 × 141 μm^2 ; 445 μm^2 × 350 μm^2	0.137; 0.339	Natural pattern	Tensile test	Strain distribution; maximum principal strain	N.A.	Home written	F_S: 51 × 51		Nicoletta et al. (2005)
Cortical bone of bovine tibias	180 μm^2 × 141 μm^2 ; 445 μm^2 × 350 μm^2	0.137; 0.339	Natural pattern	Tensile test	Principal strain	7	Home written	F_S: 24 × 18 G_S: 50; F_S: 14 × 10; G_S: 10		Nicoletta et al. (2006)
Bovine cortical bone	2.6 mm ² × 2 mm ² ; 1.3 mm ² × 1 mm ²	1.30; 0.65	Natural pattern	Compression test; nanoindentation test	Axial strain	4; 3	Home written	F_S: 60 × 60		Hoc et al. (2006)
Ovine early bone callus	23.2 mm ² × 15.4 mm ²	7.7	Powder	Compression test	Strain distribution, minimal principal distribution	N.A.	Vic-2D	F_S: 29 × 29		Thompson et al. (2007)
Cortical bone from bovine femoral shaft	8 mm ² × 8.7 mm ²	17	Airbrush	Three-point bending	Normal strains and shear strain	20	Home written	F_S: 36 × 36		Yamaguchi et al. (2011)
Bovine fibro lamellar bone	N.A.	N.A.	Airbrush	Tensile test	Axial and transversal strain		Home written	F_S: 30 × 70	Use of high-speed camera	Benecke et al. (2011)
Single trabecular of bovine femora	N.A.	N.A.	Inkjet printing	Three-point bending	Displacement and strain distribution	10	Vic-2D	N.A.	High speed photography	Jungmann et al. (2011)
<i>Whole organ – human</i>										
Human teeth	3 mm ² × 4 mm ²	3	Powder	Crack propagation	Displacement distribution	N.A.	Home written	F_S: 15 × 15	Fatigue and fracture	Zhang et al. (2007)

(Continued)

Table 2. (Continued)

Specimen	Field of view	Pixel size (μm)	Type of random pattern	Type of mechanical test	Reported quantities	Number of specimens	DIC system	DIC parameters	Note	References
Human femurs	N.A.	N.A.	Natural pattern	Sideways fall	Horizontal and vertical displacement; strain distribution	22	Home written	N.A.	Use of high-speed camera	Op Den Buijs and Dragomir-Daescu (2011)
Dried mandible	N.A.	N.A.	Airbrush	Compression test	Major principal strain	N.A.	Aramis 3D	N.A.		Tanasic et al. (2012)
Human femur	$87 \text{ mm}^2 \times 87 \text{ mm}^2$	250	N.A.	Sideways fall	Principal minimum strain	1	Strain Master	F_S: 32×32 ; G_S: 50%	Use of high-speed camera	Helgason et al. (2014)
Human vertebra	$100 \text{ mm}^2 \times 67 \text{ mm}^2$	N.A.	Airbrush	Accuracy and precision test	Principal strain	1	Istra-4D	F_S: 15×15 ; 19×19 ; 21×21 ; 25×25 ; G_S: $4,7,11,15$; C_W: $3,5,7,9,11,13,15$		Palanca, Brugo et al. (2015)
Human femur	N.A.	100	Manually applied with marker	Compression test	Principal strain	3	Vic-3D	F_S: 25×25 ; G_S: 1, 5 px	Use of high-speed DIC	Grassi et al. (2014)
<i>Whole organ – animal</i>										
Cemented total hip replacement	$19 \text{ mm}^2 \times 14 \text{ mm}^2$	9.3	N.A.	Fatigue test	Full-field displacement, strain distribution	1	Home-written	N.A.		Zhang and Arola (2004)
Chelipeds of lobster	$2 \text{ mm}^2 \times 4 \text{ mm}^2$	9.5	Airbrush	Tensile test	Displacement and strain distribution	8	Aramis 3D	F_S: 23×23 ; G_S: 10 px		Sachs et al. (2006)
Mouse tibia	$16 \text{ mm}^2 \times 12 \text{ mm}^2$	12	Airbrush	Compression test	Strain (average)	4	Aramis 3D	F_S: 19×19 ; G_S: 9		Sztefek et al. (2010)
Fresh ovine femur	N.A.	N.A.	Airbrush	Compression test	Strain distribution	N.A.	Vic-3D	N.A.		(Ghosh et al. 2012)
Rat femora	N.A.	N.A.	Airbrush	Compression test till failure	Principal strain	9	Vic-3D	N.A.		Amin Yavari et al. (2013)
Mouse tibia	$15 \text{ mm}^2 \times 12 \text{ mm}^2$	6	Airbrush	Compression test	Max and average strain	3	Aramis 3D	F_S: 19×19 ; overlap: 20%		Carriero et al. (2014)
<i>Synthetic</i>										
Dental composite	N.A.	N.A.	Airbrush	Curing process	Axial and transversal strain	10	Strain Master	N.A.		Li et al. (2009)
Composite femur	25 area of 5 mm^2	50	Airbrush	Press/flection test	Strain (sensitivity/experimental error)	N.S	Vic-3D	N.A.		Dickinson et al. (2011)
Osseo integrated trans-femoral implant system	N.A.	47	N.A.	Bending test	Displacement and strain distribution	12	Vic-3D	F_S: 27×27 ; G_S: 10 px; C_W: 150 px ²		Thompson et al. (2011)
Dental composited	N.A.	N.A.	Powder	Curing process	Axial and transversal displacement	32	Vic-2D	F_S: 21×21		Chuang et al. (2011)
Acrylic resin mandibular with and without implant	$50 \text{ mm}^2 \times 37.5 \text{ mm}^2$	35	Airbrush	Three-point bending	Strains in horizontal direction and in-plane shear strain	N.A.	Strain Master	N.A.		Trossi et al. (2011)

Composite hemi-pelvis	36 area of 5 mm ² × 5 mm ²	N.A.	Airbrush	Compression test	Displacement distribution; principal strain	N.A.	Vic-3D	N.A.	Dickinson et al. (2012)
Acrylic resin mandibular with and without implant	50 mm ² × 37.5 mm ²	35	Airbrush	Three-point bending	Strains in horizontal direction and in-plane shear strain	N.A.	Strain Master	N.A.	Tirossi et al. (2012)
Composite femur	115 mm ² × 57 mm ²	200	Airbrush	Sideways fall	Displacement distribution; minimum principal strain	20	Strain Master	N.A.	Gilchrist et al. (2013)
Composite femur	N.A.	N.A.	Airbrush	Press/flection test	Principal strain	6	Vic-3D	N.A.	Grassi et al. (2013)
Composite femur	N.A.	N.A.	Airbrush	Compression test	Principal strain	6	Vic-3D	N.A.	Vaananen et al. (2013)

Notes: With each subsection, references are listed in chronological order.

N.A = information not available.

F_S = facet size.

G_S = grid spacing.

C_W = computation window.

Istra-4D by Dantec Dynamics (Skovlunde, Denmark), Aramis 3D by GOM (Braunschweig, Germany), Vic-2D and Vic-3D by Vision Solution (Irvine, California, USA), StrainMaster and DaVis by LaVision (Goettingen, Germany).

ProAnalyst by Xcited (Woburn, Maine, USA).

Rapid Correlation by XStream Software (Ottawa, Ontario, Canada).

of the facet size is remarkable (Lava et al. 2009). The facet size must be defined according to: the specimen size (or the field of view), the size of the speckles, and the strain gradients expected based on the loading conditions and the anatomy (Carriero et al. 2014; Freddi et al. 2015).

The facet should be larger than speckle dots, to allow detection of small displacements, in relationship to the granularity of the speckle pattern (Sutton et al. 2009). However, the facet should not be unnecessarily large, to avoid loss of resolution (Lionello & Cristofolini 2014).

4.2. Grid spacing

This parameter indicates the distance between two consecutive facets. It describes the density of facets in the measurement window: the smaller the grid spacing, the larger the number of facets (at a higher computational cost). The influence of the grid spacing on the precision and accuracy of the computed displacement field is minimal (Lava et al. 2009). Conversely, the overlap provides advantages in terms of precision and accuracy of the computed strain field. The density of measurement points should be selected based on the test details (type of specimen, field of view, pattern and strain gradient). For an expected uniform strain (e.g. long bone in bending) larger grid spacing can be preferable. Conversely, if high strain gradients are expected (e.g. specimens with complex geometry), a smaller grid spacing is necessary (Sutton et al. 2009, Palanca, Brugo et al. 2015).

4.3. Strain computation window

Once the displacements have been computed for each facet, the strain field is computed by derivation. While in principle 2 × 2 facets are sufficient to compute the local strain, larger windows are often used to attenuate the noise in the derived strain field. While larger strain computation windows reduce the noise in the DIC-computed strain distribution, this also may result in an attenuation of existing strain gradients, which can be detrimental when analyzing specimens with an irregular geometry (which often occurs with anatomical specimens). This effect is thus similar to the effect of grid spacing (Sutton et al. 2009, Palanca, Brugo et al. 2015).

4.4. Validity quote

The validity quote represents the tolerance for computing/ignoring the strain in a certain region: if the number of valid neighbouring points is below the threshold, the software does not evaluate the strain. A high level of the validity quote means that strains are computed only where redundant information is available, thus providing a more

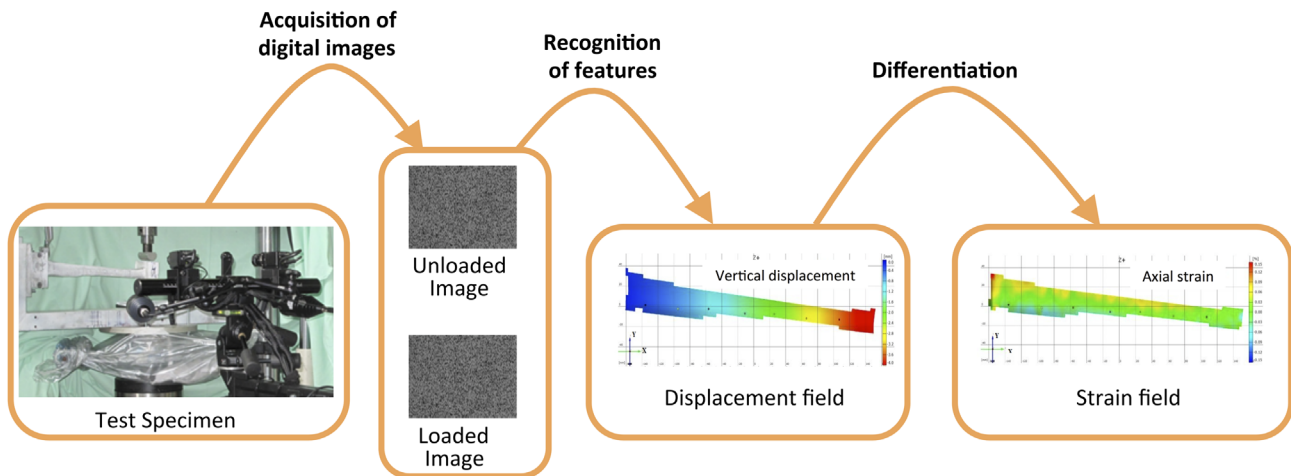


Figure 1. Workflow of DIC displacement and strain measurement: as an example, a 3D-DIC arrangement was used to investigate a human tibia.

Table 3. Summary of the main potentialities and limitations of DIC.

Advantages	Disadvantages
<ul style="list-style-type: none"> • Full-field measurement of displacement/strain • For any size and material of specimens • Determination of strain gradient and stress concentrators • Both for small and large deformation • Usable <i>in vivo</i> • Synergies with FE • Not invasive* 	<ul style="list-style-type: none"> • Less accurate and precise than others measurements techniques • Need of a carefully optimization for the specific application • Not real-time • Need of optical access to the specimen • Requires surface preparation*

*In most cases, a surface preparation is required. It is a layer of paint or powder fixed on the surface. Sometimes, the natural pattern is usable to track the deformation of the surface.

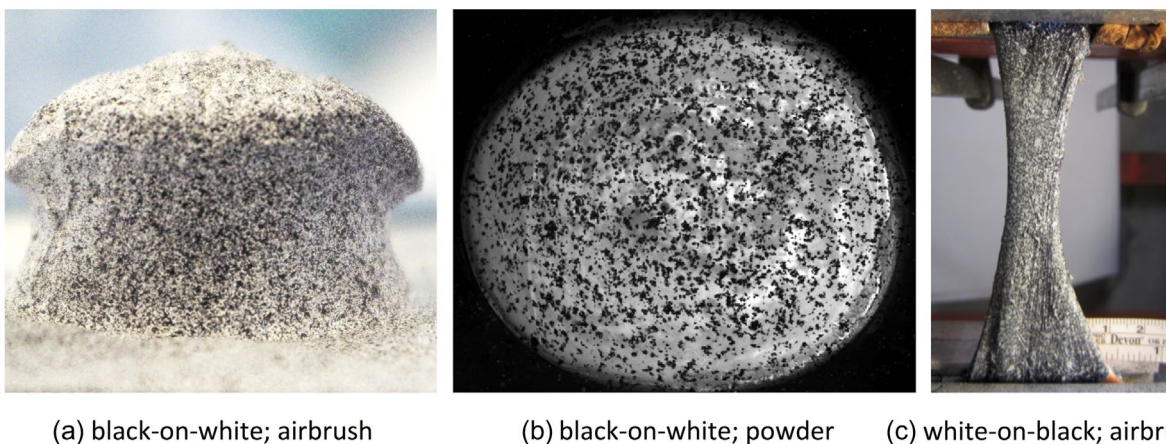


Figure 2. Example of specimens with different speckle patterns: (a) black-on-white speckle pattern created with the airbrush airgun technique on a porcine vertebral body; (b) black-on-white speckle pattern created with the powder technique on a bovine cornea (picture courtesy of Dr Brad L. Boyce, (Boyce et al. 2008)); (c) Speckle pattern created with airbrush airgun technique, white-on-black, on a human Achilles tendon (picture adapted from (Luyckx et al. 2014)).

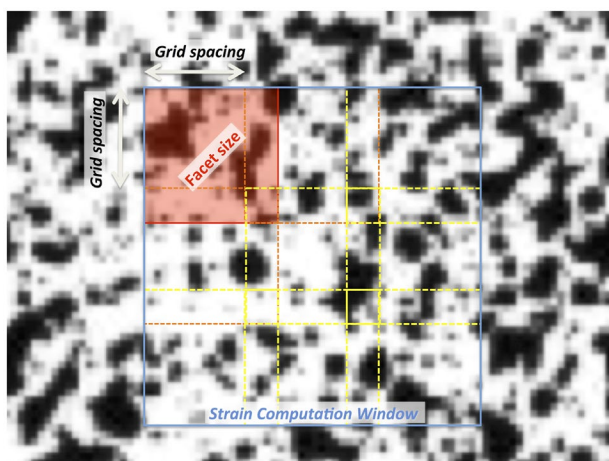


Figure 3. Detail of the specimen surface prepared with a random speckle pattern, as seen after acquisition as a digital image (i.e. discretized in pixels).

Notes: The DIC software parameters are illustrated: to compute the displacement field, the digitized image is divided in sub-images (facets, 20×20 pixels in this case); a grid spacing of 15 pixels is used in this case (resulting in a partial overlap of 5 pixels); a larger area (computation window, 3×3 facets in this case) is used to compute the strain field.

reliable strain value. If the specimen has a complex geometry (i.e. a vertebra, or a pelvis), a lower threshold might be necessary, resulting in less reliable strain estimates.

4.5. Filtering

In general, DIC allows obtaining very precise displacement fields (i.e. affected by very low noise, typically sub-pixel). However, as derivation acts as the opposite of a filter (enhancing the noise in the displacement field computed from noisy digital images), the strain field is generally affected by large random error. Filtering can be applied to the digital images, to the DIC-computed displacement field, and/or to the DIC-computed strain field (Baldoni et al. 2015). There are several filters that mainly differ in the intensity of attenuation, and filtering strategy (whether local or global). However, this also smoothens any gradient or stress/strain concentration, resulting in a loss of information.

For a homogeneous deformation (i.e. in the diaphysis of a long bone, or a tendon under tension) a smoothing spline can be successfully used to attenuate the noise by averaging the results over the field of view. Larger averaging areas are associated with more severe loss of information (Lava et al. 2010). Conversely, when the specimen is subject to high strain gradients (i.e. an irregular bone such as a vertebra, or a complex structure such as the sclera) a local filtering, should be preferred (at the cost of noisier results, (Wang et al. 2012)). Alternatively, strain can be

computed by means of an FE solver, where DIC-measured displacements are imposed to the FE nodes (Evans & Holt 2009). The continuum assumption (which is intrinsic to FE modelling), acts as a low-pass filter.

5. Errors affecting DIC measurements in biomechanics

5.1. Accuracy and precision

It is important to distinguish between systematic error (bias of the average, resulting in lack of accuracy) and random error (large standard deviation, resulting in lack of precision). In fact, accuracy and precision of the DIC measurements cannot be taken for granted if the measurement system and the numerical processing have not been optimized and validated (Figure 4). The errors affecting displacement and strain are originally induced by the overall quality of the native images. The DIC-computed displacement field is less sensitive to modifications of software parameters; their effect is larger on strains (Nicolella et al. 2001; Palanca, Brugo et al. 2015). Accuracy and precision of the DIC in computing the displacements are in the order of 0.01 pixel (Nicolella et al. 2001; Zhang & Arola 2004; Amiot et al. 2013); with some optimizations errors can be further reduced (Barranger et al. 2010). DIC-computed strains are generally quite accurate (systematic errors of the order of few microstrains are negligible in most biomechanical applications). Conversely, large noise usually affects DIC-computed strains: a precision of some hundreds of microstrain can be achieved only under optimal conditions.

5.2. Errors due to the pattern

The DIC analysis relies on the presence of a suitable pattern on the specimen surface. In order to evaluate the errors related to the morphology of the pattern, digital images of the speckle patterns were virtually translated (Haddadi & Belhabib 2008), numerically deformed (Lecompte et al. 2006), correlated in a zero-strain condition (Carriero et al. 2014). An unsuitable speckle pattern is likely to make the correlation impossible at some facets, reducing the number of measurements points (Haddadi & Belhabib 2008). An optimal ratio exists between the facet size and the mean speckle size to reduce errors affecting DIC-computed displacements (Lecompte et al. 2006, 2007). They also showed that a limited scatter of speckle sizes yields more accurate displacement measurements, and that larger dots result in larger random errors in the displacement field. The differences between black-on-white and white-on-black speckle patterns are negligible in terms of measurement quality (Barranger et al. 2010). A clear relationship exists

between the measurement error and the uniqueness of the pattern, which depends on the speckle size and shape, and on the facet size (Crammond et al. 2013). The airbrush airgun method provides a better control of the dots dimension compared to the use of powder (Myers et al. 2010). Even if an airbrush airgun can only to a limited extent be adjusted to produce the desired speckle dots (Crammond et al. 2013), the performance of DIC is quite robust and tolerant (Wang et al. 2012).

5.3. Errors affecting the acquired images

Random errors affect the images acquired by the digital camera, such as thermal noise (or dark noise), excess noise due to the CCD sensor and electromagnetic noise of the relative measurement chain (Freddi et al. 2015). Moreover, a source of systematic error in 2D-DIC derives from out-of-plane displacements of the specimen during loading. 2D-DIC is often chosen in investigations at the tissue level (Sutton, Yan et al. 2008, Pan et al. 2013). They explained the combined effect of the out-of-plane motion of the tested object surface and of the cameras.

5.4. Errors due to the correlation process

Suboptimal choice of the software parameters can result in large noise, or, conversely, could hide existing strain gradients (Baldoni et al. 2015). The optimal parameters can be identified through virtually imposed displacement tests (Haddadi & Belhabib 2008). Numerically deformed images were prepared to evaluate the accuracy and precision in the displacement field, and identify the optimal parameters (Lava et al. 2009, 2010, 2011) (Wang et al. 2012). A zero-strain test was applied on a vertebra (Figure 4) to investigate the software parameters to estimate the accuracy and precision (Palanca, Brugo et al. 2015).

5.5. Recommendations to minimize measurement errors in biomechanical applications

It is possible and to some extent mandatory to validate DIC measurements by comparison against independent measurements: (Zhang & Arola 2004; Sutton Ke et al. 2008, Gilchrist et al. 2013) compared the DIC-computed strains against single strain gauges. A more extensive validation may include the use of specimens with known material properties, subjected to well-defined loading conditions (Zhang & Arola 2004; Sutton, Ke et al. 2008, Gilchrist et al. 2013). Moreover, preliminary tests to identify the spatial displacements could help in avoiding out-of-plane artefacts in a 2D-DIC.

To optimize the speckle pattern for biological specimens (Lionello & Cristofolini 2014; Lionello et al. 2014;

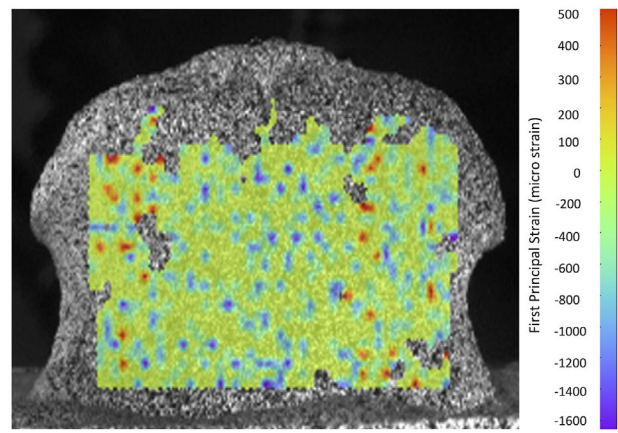


Figure 4. Example of errors affecting the DIC-computed strain distribution. A porcine vertebra was examined in a zero-strain condition.

Notes: Strains were computed with DIC software with default (i.e. not optimized) settings. Any strain readout different from zero is due to errors (a combination of systematic error and random error).

Palanca, Brugo et al. 2015) proposed a factorial design to adjust the airbrush settings so as to a pattern having the desired average speckle size with minimal scatter.

The lens distortion generates a systematic error, which can be partially compensated through dedicated algorithms (Yoneyama 2006), or an appropriate calibration (Patterson et al. 2007; Sebastian & Patterson 2012). Such artefacts can be completely eliminated with telecentric lenses (Pan et al. 2013), or by exploiting the central portion of the lens angle (Palanca, Brugo et al. 2015). An in-house smart solution consists in performing 3D deformation measurements with a single camera using a biprism to avoid distortion of the images (Genovese, Casaletto et al. 2013; Genovese, Lee et al. 2013). The illumination must be stable and uniform to reduce the noise and obtain better native images. Moreover, due to the nature of biological specimens, cold light illumination is preferable (i.e. using LED technology). Noise and its influence can be somehow reduced, but not completely eliminated, with high-performance hardware (i.e. lenses, cameras, frame grabber, etc.).

To reduce correlation errors due to unsuitable settings, it is important to have a provisional estimate of the expected strain gradients. In case of homogeneous deformation a large facet size, large grid spacing and large computation window are able to produce accurate and precise measurement with limited computation cost (Sutton et al. 2009). Conversely, stress/strain concentrations should be investigated with a high spatial resolution (i.e. small facets and computation windows), to avoid loss of detail.

Filtering can help reduce the noise in the DIC-computed strains. However, filtering should be used with extreme caution to avoid loss of information in high-gradient

regions, such as anatomical specimens with an irregular geometry, or in highly inhomogeneous tissues (Baldoni et al. 2015). A careful optimization of the entire measurement chain can reduce the errors (Figure 5) and provide more accurate and precise outputs (Palanca, Brugo et al. 2015).

6. Examples of biomechanical applications

Big potentiality of DIC lies in its suitability to investigate different kinds of materials, such as soft and hard biological tissue, independently their mechanical behaviour (brittle/ductile, isotropic/anisotropic, homogeneous/inhomogeneous), for small or large deformation (Sutton et al. 2009).

6.1. Applications to soft tissue

Before the introduction of DIC, strain in soft tissue structures has been initially measured by means of extensometers (Larrabee 1986; Nagarkatti et al. 2001). This method significantly perturbs the specimen under observation, both in terms of local stiffening and notching. A better alternative is based on optical extensometers (i.e. (Holzapfel 2006; Weisbecker et al. 2012)). The main limitation of optical extensometers is that they track the displacement of only two points in the specimen. Therefore, the strain field between such points is averaged, with no information about the local strain distribution. Furthermore, most optical techniques tend to loose correlation when large displacements are involved, which often occurs with soft tissues. DIC overcomes such problems, opening possibilities to new measurements and new data in the experimental tests (Table 1). For example, DIC opened the way to measurements on micrometric scales (tissue level).

DIC enabled improvements in the field of microindentation. Originally, indentation focused only on the force-indentation relationship. DIC allows measuring the surface

deformation around the point of load application. This methodology was assessed on a silicon gel (Moerman et al. 2009) and on a porcine liver (Ahn & Kim 2010). Single-camera-DIC combined with a radial-fringe-projection was used to measure the displacement field in the indentation tests on porcine ventricle (Genovese et al. 2015). As the reliability of DIC with microindentation has been proven *in vitro*, this technique has the potential to be deployed *in vivo* for future diagnostic purposes.

In vitro application of DIC to measure the strain distribution in various components of the cardiovascular system is extremely important, for potential its impact to improve the understanding of pathologies, and deliver better treatment. However, the state of stress/strain is difficult to measure, because of the inherent pseudoelastic nature, the small dimensions of the specimens, and the difficulty in reproducing the physiological working condition. Initially, bovine aorta specimens were investigated by means of DIC by Zhang et al. (2002a): Poisson's ratio was determined from the displacements, and the corresponding strains up to 40%, in the axial and circumferential directions. This work was based on simplified boundary conditions: the specimens were loaded in a uniaxial tensile test, far from the physiological conditions. Additional experiments were conducted with silicone rubber sheets, providing a validation of DIC under large strains. Later, other works included an improved resemblance to the physiological condition. Mice carotid arteries were subjected to a pressure test to identify significant variations in constitutive material response (Sutton, Ke et al. 2008). This test was performed using a microscopic 3D-DIC, with a field of about 0.2 mm². Due to the 3D anatomy, only a restricted region of the surface was investigated. The entire surface of a mice carotid was investigated out using a conic mirror, while a single camera was moved (Genovese et al. 2011; Genovese & Humphrey 2015). The

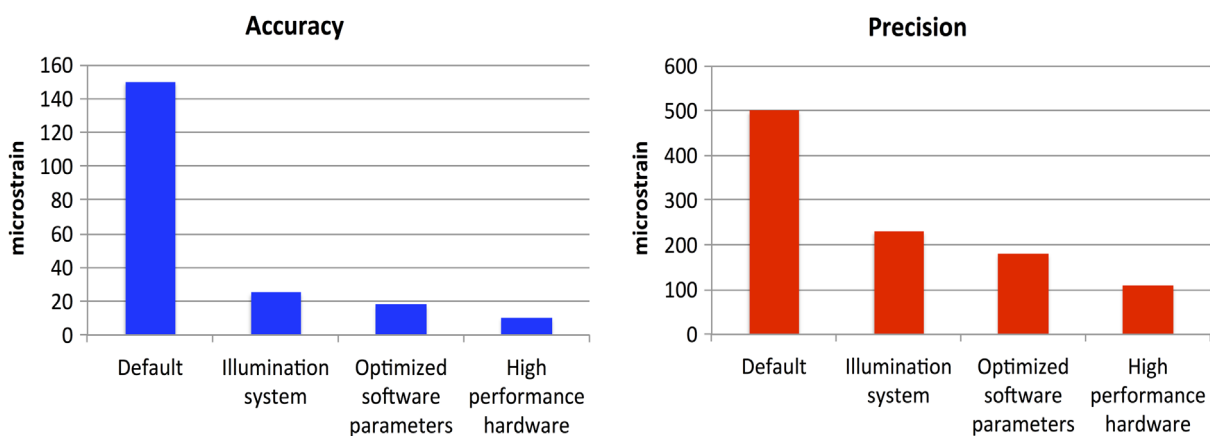


Figure 5. Plots showing how the systematic error and the random noise were dramatically high if no special care was taken to reduce them, and how effective an optimization following the principles of DOE can be, to improve precision and accuracy (Palanca, Brugo et al. 2015).

distribution of mechanical properties was obtained from the strain field, exploiting an inverse material characterization. As this method allows measuring displacements and strains on the entire surface, complex pathological conditions such as abdominal aortic aneurysms could be investigated (Genovese et al. 2012). The anisotropy of tissue-engineered heart valves was investigated with indentation tests at a microscopic scale (Cox et al. 2008).

A pioneering rudimentary DIC system allowed evaluating the strain distribution in the human cornea by measuring the *in vitro* displacement of only few (6) discrete particles (Shin et al. 1997). In order to understand the non-linear viscoelastic and anisotropic behaviour of the cornea, a 3D-DIC was used (Boyce et al. 2008). Bovine corneas were constrained in a custom pressurization chamber and loaded with physiological and pathological pressure. The potentialities of 3D-DIC were exploited to measure the out-of-plane displacements and to obtain the pressure-displacement response. The response at various pressure rates and the creep at different pressures of the bovine posterior sclera were investigated (Myers et al. 2010). A consolidated protocol to measure the spatial displacement field during an inflation test was used for an in-depth investigation of the behaviour of physiological and pathological human posterior sclera (Coudrillier et al. 2012, 2013). A system where the camera can be rotated by 90 degrees around two orthogonal axes (sequential-DIC) allows improving the out-of-plane resolution of a single camera, without losing sensitivity (Pyne et al. 2014). They used sequential-DIC for mapping the optic nerve head deformation. As sequential-DIC requires some time to acquire the images from different angles, it cannot be used for time-critical experiments such as measuring viscoelastic properties. The advent of DIC enabled the incorporation of loading conditions that better replicate the complex *in vivo* mechanical environment in the eye structure, compared to the crude simplifications of the past (uniaxial tests (Boyce et al. 2007)).

Cartilage tissue specimens (1-mm cubes) were subjected to unconfined compression tests; 2D-DIC was used to measure the equilibrium modulus and the Poisson ratio (Wang et al. 2002, 2003). Similarly, the Poisson ratio was measured at the tissue level in tension for the human patellar cartilage (Narmoneva 2002; Zhang et al. 2005).

Intervertebral discs are difficult to study, both for their mechanical behaviour and for their anatomical position. Traditionally (Causa et al. 2002; Panjabi 2007) the force-displacement curve of functional spinal units was extracted from displacement transducers under uni- or multi-axial simulators. The strain distribution in the discs was measured with 3D-DIC at the organ level under simulated physiological loading (Spera et al. 2011).

The distribution of strain in the entire human Achilles tendon was examined through DIC (Luyckx et al. 2014), while in the past only the average strain could be assessed by means of extensometers. An image correlation process was applied to dynamic ultrasound images to measure the *in vivo* strain distribution in mice tendon (Okotie et al. 2012). This technique exploited the “natural” speckle pattern of ultrasound images.

The biomechanics of bovine hoof has been investigated in uniaxial tension using DIC, so as to obtain a full-field description of the axial strain distribution (Zhang & Arola 2004). The strain gradients observed indicated an inhomogeneous distribution of the mechanical properties, which would otherwise be difficult to assess.

The interplay between the uterine cervix tissue and its macroscopic mechanical properties was investigated with DIC (Myers et al. 2008). Strain distributions in the range from 5 to 30% were measured with DIC, and plotted against stress.

Recent works were done on porcine uterosacral and cardinal ligaments in uni-axial (Tan et al. 2015) and bi-axial (Becker & De Vita 2015) loading conditions, deploying a simplified DIC (a limited number of poppy seeds used as markers). They determined the mechanical properties (elastic moduli, ultimate tensile strength and strain) of the two major ligaments that support uterus, cervix and vagina. The bi-axial test, moreover, investigated deeply the orthotropic behaviour of these ligaments, formulating a new three-dimensional constitutive model.

The spatial deformation of the vocal folds was measured by means of DIC (Spencer et al. 2008; Kelleher et al. 2010). This study focused on the superior surface of a synthetic model of the vocal folds sprayed with a speckle pattern. To extend this promising technique to clinical laryngoscopic evaluations, a non-toxic speckle pattern would be required. DIC was used *in vitro* to evaluate the spatial deformation field for an entire vocal ligament. FE models, based on the DIC-derived material properties, were created to evaluate how variations of cross section, inhomogeneity and anisotropy affect the fundamental frequency of vibration (Kelleher et al. 2010).

An area where DIC outperforms most other strain measurement techniques is that of *in vivo* measurements, thanks to its limited invasiveness. *In vivo* applications of DIC are hindered by a number of factors: difficulty/impossibility to create a dedicated speckle pattern, and limited control on the boundary conditions. The displacement of a non-linear elastic, viscoelastic, anisotropic material, highly variable and sensitive to the environment condition, such as the human skin was measured *in vivo* using DIC under large deformation, enabling the creation of a library of material properties (Evans & Holt 2009). Fast and

accurate measurement of the displacements and strain of the heart during cardiac surgery can help assessing the best strategy: DIC (exploiting the natural pattern on the myocardium) was adopted in the surgical theatre during a cardiopulmonary bypass surgery (Hokka et al. 2015). DIC was applied to ultrasound breast images to identify cancerous tissue, based on its deformation and stiffness (Han et al. 2012). DIC with ultrasound images has also been used to measure *in vivo* deformation in tendons (Okotie et al. 2012) and lower limb muscles (Affagard et al. 2014).

6.2. Applications to hard tissue

Historically, the main way to measure strain in hard tissues was by means of strain gauges (Cristofolini & Viceconti 1997; Cristofolini, Conti et al. 2010; Yang et al. 2011; Cristofolini et al. 2013). However, the reinforcement effect of strain gauges may not be negligible (Little et al. 1990; Ajovalasit & Zuccarello 2005). Strain gauges are sometimes too large when compared to the scale at which strains gradients are evaluated in biological tissues (Cristofolini et al. 1997; Nicoletta et al. 2001; Amin Yavari et al. 2013). Furthermore, strain gauges only measure at the discrete points where they are attached. Extensometers have sometimes been used to measure deformation in bone specimens, e.g. (Keaveny et al. 1997). Similarly to soft tissue, extensometers may induce micro-damage in bone, and measure the average strain over the gauge length. Relevance of transmission photoelasticity to bone testing is limited by the fact that model materials such as araldite are homogeneous and isotropic. With reflection photoelasticity real bone can be tested, but large errors arise due to the reinforcement effect (Cristofolini et al. 1994, 2003). An overview of applications of strain gauges, in-fibre Bragg grating sensors, DIC and digital volume correlation (DVC) was recently published (Grassi & Isaksson 2015).

DIC shows its benefits also with hard tissue, allowing operating at different dimensional scales (Table 2): from small specimens (tissue level), such as cortical bone (Hoc et al. 2006), teeth (Gao et al. 2006), up to large specimens (organ level), such as whole bones (Tayton et al. 2010). In this case small strains are involved, never exceeding 10,000 microstrain (Bayraktar et al. 2004).

The problem of characterizing cortical bone at the tissue level (Haversian system) to assess local phenomena, such as micro-damage or bone remodelling, was solved with DIC (Nicoletta et al. 2001; Hoc et al. 2006). Single trabeculae of cancellous bone have been investigated with DIC and a high-speed camera in a three-point-bending test (Jungmann et al. 2011).

A whole-organ investigation was carried out on teeth (few millimetres) to optimize the stiffness and load transfer in dental implants (Tioosi et al. 2011). DIC and strain

gauges were used on mouse tibias under axial compression (Sztefek et al. 2010). It was concluded that the spatial resolution of the strain gauges was inadequate to measure the localized peak strains identified by DIC. Similarly, (Vaananen et al. 2013) showed the effectiveness of DIC in identifying the location and modality of fracture in bones (in this preliminary study composite femurs were used). Strains measured with DIC at selected regions were used to validate an FE model of the same composite femur built from computed tomography (Dickinson et al. 2011). This research was further extended by (Grassi et al. 2013), who performed a much larger number of DIC measurements on similar composite femurs. A similar work was carried out on cadaver femurs: a high-speed cameras were used to measure strain and fracture with 2D-DIC, and validate the corresponding FE models (Op Den Buijs & Dragomir-Daescu 2011). This approach was further extended to 3D-DIC using two high-speed cameras (Grassi et al. 2014; Helgason et al. 2014). Due to their limited resolution (1 Megapixel or lower, depending on the frame rate), high-speed cameras were originally introduced to biomechanical investigations only to qualitatively investigate fracture (Cristofolini et al. 2007; de Bakker et al. 2009; Juszczyk et al. 2011; Schileo et al. 2008; Zani et al. 2015). High-speed cameras with sufficient resolution to be integrated in a DIC system became available only recently.

A preliminary application to the human vertebra was recently published, where the methods were fine tuned to minimize errors (Palanca, Brugo et al. 2015).

7. Synergies with FE in biomechanics

Another important feature of DIC is its ability to integrate with FE models, in different ways (Babuska & Oden 2004; Jones & Wilcox 2008, Cristofolini, Schileo et al. 2010):

- (1) Experimental identification of model parameters: the high complexity involved in FE models (often including patient-specific detail, inhomogeneous material properties, non-linear interfaces, etc.) requires experimental measurements to identify the input parameters.
- (2) Experimental validation of model predictions: as reliability of numerical predictions cannot be taken for granted, quantitative comparison with experimental data is necessary. DIC (if properly optimized) has a similar accuracy, but more noise than strain gauges. However, DIC can provide full-field information. For instance, DIC was used to validate FE models of the proximal femur for the prediction of strains and fracture, both qualitatively (Helgason et al. 2014) and quantitatively (regression between DIC-measured and

- FE-computed stiffness and strain (Dickinson et al. 2011; Op Den Buijs & Dragomir-Daescu 2011; Grassi et al. 2013)).
- (3) Use of numerical models to improve the experiment: the synergy between a local approach (implemented in most DIC software) and a global approach (FE) can be exploited to reduce the errors in DIC-computed strain field. In fact, usually low-pass filters are used to reduce the noise in the strain maps obtained by derivation of the displacements (Baldoni et al. 2015). This can result in loss of information due to the smoothing of existing gradients. Alternatively, strain can be computed by means of an FE solver, where DIC-measured displacements are imposed to the FE nodes (Evans & Holt 2009). The continuum assumption (which is intrinsic to FE modelling), acts as a low-pass filter.
 - (4) Use of numerical models for inverse material characterization, based on experimental measurements: integration of numerical and experimental methods allows non-destructive assessment of mechanical properties that are otherwise difficult to measure experimentally. For instance, to investigate the mechanical response of the skin, *in vivo* strain under point loading was measured by DIC; such measurements were fed into an FE model to estimate the hyperelastic parameters (Evans & Holt 2009). Similarly, specimen-specific FE models of the sclera were fed with DIC-measured quantities (Coudrillier et al. 2013).

8. Other image correlation tools

DIC allows calculating the displacement and/or strain only on the surface of the specimens. An important step forward in the characterization of biological structures consists in measuring displacement and strain fields on entire volumes (Roberts et al. 2014; Freddi et al. 2015). The concept of DVC was introduced by (Bay, Smith et al. 1999, Smith et al. 2002) as a natural extension of DIC to a three-dimensional domain. With the rapid improvement of micro-focus computed tomography (micro-CT), DVC has gained increasing attention as a powerful tool to examine full-field deformations in trabecular bone (Liu & Morgan 2007; Dall'Ara et al. 2014; Gillard et al. 2014; Palanca, Tozzi et al. 2015), cortical bone (Dall'Ara et al. 2014; Palanca, Tozzi et al. 2015), whole bones (Hussein et al. 2012, 2013), cellular scaffolds (Madi et al. 2013) and bone-cement interface (Tozzi et al. 2014).

9. Conclusions

This review has shown the potential usefulness of DIC as a full-field, contactless and versatile technique. In fact successful biomechanical applications of DIC can be found at different dimensional scales (from the microscopic tissue level, to macroscopic organ-level specimens), on a wide range of biological specimens (both soft and hard tissue) and for a variety of tests, including fracture.

DIC can measure displacements with very high accuracy and precision. However, to obtain accurate and precise measurement of strain, great care is needed to optimize the surface preparation, and the hardware and software settings. Thanks to the versatility of DIC, it can be foreseen that more and more application will be developed in biomechanics in the forthcoming years, both *in vitro* and *in vivo*.

Acknowledgements

The authors wish to thank Dr Thomas Luyckx and Dr Brad L. Boyce for providing the pictures reproduced in Figure 2.

Disclosure statement

No potential conflict of interest was reported by the authors.

ORCID

Marco Palanca  <http://orcid.org/0000-0002-1231-2728>
Luca Cristofolini  <http://orcid.org/0000-0002-7473-6868>

References

- Affagard JS, Bensamoun SF, Feissel P. 2014. Development of an inverse approach for the characterization of *in vivo* mechanical properties of the lower limb muscles. *J Biomech Eng.* 136. doi: 10.1115/1.4028490
- Ahn B, Kim J. 2010. Measurement and characterization of soft tissue behavior with surface deformation and force response under large deformations. *Med Image Anal.* 14:138–148.
- Ajovalasit A, Zuccarello B. 2005. Local reinforcement effect of a strain gauge installation on low modulus materials. *J Strain Anal Eng Des.* 40:643–653.
- Amin Yavari S, van der Stok J, Weinans H, Zadpoor AA. 2013. Full-field strain measurement and fracture analysis of rat femora in compression test. *J Biomech.* 46:1282–1292.
- Amiot F, Bornert M, Doumalin P, Dupré JC, Fazzini M, Orteu JJ, Poilâne C, Robert L, Rotinat R, Toussaint E, Watrissse B, Wienin JS. 2013. Assessment of digital image correlation measurement accuracy in the ultimate error regime: main results of a collaborative benchmark. *Strain.* 49:483–496.
- Babuska I, Oden JT. 2004. Verification and validation in computational engineering and science: basic concepts. *Comput Methods Appl Mech Eng.* 193:4057–4066.
- de Bakker PM, Manske SL, Ebacher V, Oxland TR, Crompton PA, Guy P. 2009. During sideways falls proximal femur fractures

- initiate in the superolateral cortex: evidence from high-speed video of simulated fractures. *J Biomech.* 42:1917–1925.
- Baldoni, J, Lionello G, Zama F, Cristofolini L. 2015. Comparison of different strategies to reduce noise in strain measurements with digital image correlation. *Meas Sci Technol* (under revision).
- Barranger Y, Doumalin P, Dupré JC, Germaneau A. 2010. Digital image correlation accuracy: influence of kind of speckle and recording setup. *EPJ Web Conf.* 6:31002.
- Bay BK. 1995. Texture correlation: a method for the measurement of detailed strain distributions within trabecular bone. *J Orthop Res.* 13:258–267.
- Bay BK, Smith TS, Fyhrie DP, Saad M. 1999. Digital volume correlation: three-dimensional strain mapping using X-ray tomography. *Exp Mech.* 39:217–226.
- Bay BK, Yerby SA, McLain RF, Toh E. 1999. Measurement of strain distributions within vertebral body sections by texture correlation. *Spine* 24:10–17
- Bayraktar HH, Morgan EF, Niebur GL, Morris GE, Wong EK, Keaveny TM. 2004. Comparison of the elastic and yield properties of human femoral trabecular and cortical bone tissue. *J Biomech.* 37:27–35.
- Becker WR, De Vita R. 2015. Biaxial mechanical properties of swine uterosacral and cardinal ligaments. *Biomech Model Mechanobiol.* 14:549–560.
- Benecke G, Kerschnitzki M, Fratzl P, Gupta HS. 2011. Digital image correlation shows localized deformation bands in inelastic loading of fibrolamellar bone. *J Mater Res.* 24:421–429.
- Boyce BL, Jones RE, Nguyen TD, Grazier JM. 2007. Stress-controlled viscoelastic tensile response of bovine cornea. *J Biomech.* 40:2367–2376.
- Boyce BL, Grazier JM, Jones RE, Nguyen TD. 2008. Full-field deformation of bovine cornea under constrained inflation conditions. *Biomaterials.* 29:3896–3904.
- Bruck HA, McNeill SR, Sutton MA, Peters WH. 1989. Digital image correlation using Newton–Raphson method of partial differential correction. *Exp Mech.* Sept; 261–267.
- Brunon A, Bruyère-Garnier K, Coret M. 2011. Characterization of the nonlinear behaviour and the failure of human liver capsule through inflation tests. *J Mech Behav Biomed Mater.* 4:1572–1581.
- Carriero A, Abela L, Pitsillides AA, Shefelbine SJ. 2014. *Ex vivo* determination of bone tissue strains for an *in vivo* mouse tibial loading model. *J Biomech.* 47:2490–2497.
- Causa F, Manto L, Borzacchiello A, De Santis R, Netti PA, Ambrosio L, Nicolais L. 2002. Spatial and structural dependence of mechanical properties of porcine intervertebral disc. *J Mater Sci Mater Med.* 13:1277–1280.
- Chu TC, Ranson WF, Sutton MA, Peters WH. 1985. Applications of digital-image-correlation techniques to experimental mechanics. *Exp Mech.* 25:232–244.
- Chuang SF, Chang CH, Chen TY. 2011. Contraction behaviors of dental composite restorations—finite element investigation with DIC validation. *J Mech Behav Biomed Mater.* 4:2138–2149.
- Coudrillier B, Boote C, Quigley HA, Nguyen TD. 2013. Scleral anisotropy and its effects on the mechanical response of the optic nerve head. *Biomech Model Mechanobiol.* 12:941–963.
- Coudrillier B, Tian J, Alexander S, Myers KM, Quigley HA, Nguyen TD. 2012. Biomechanics of the human posterior sclera: Age- and glaucoma-related changes measured using inflation testing. *Invest Ophthalmol Vis Sci.* 53:1714–1728.
- Cox MA, Driessen NJ, Boerboom RA, Bouten CV, Baaijens FP. 2008. Mechanical characterization of anisotropic planar biological soft tissues using finite indentation: experimental feasibility. *J Biomech.* 41:422–429.
- Crammond G, Boyd SW, Dulieu-Barton JM. 2013. Speckle pattern quality assessment for digital image correlation. *Opt Lasers Eng.* 51:1368–1378.
- Cristofolini L, Brandolini N, Danesi V, Juszczuk MM, Erani P, Viceconti M. 2013. Strain distribution in the lumbar vertebrae under different loading configurations. *Spine J.* 13:1281–1292.
- Cristofolini L, Conti G, Juszczuk M, Cremonini S, Sint Jan S, Viceconti M. 2010. Structural behaviour and strain distribution of the long bones of the human lower limbs. *J Biomech.* 43:826–835.
- Cristofolini L, Cappello A, Toni A. 1994. Experimental errors in the application of photoelastic coatings on human femurs with uncemented hip stems. *Strain.* 30:95–104.
- Cristofolini L, Juszczuk M, Martelli S, Taddei F, Viceconti M. 2007. *In vitro* replication of spontaneous fractures of the proximal human femur. *J Biomech.* 40:2837–2845.
- Cristofolini L, McNamara B, Freddi A, Viceconti M. 1997. *In vitro* measured strains in the loaded femur: quantification of experimental error. *J Strain Anal Eng Des.* 32:193–200.
- Cristofolini L, Metti C, Viceconti M. 2003. Strain patterns induced by press-fitting and by an external load. *J Strain Anal.* 38:290–301.
- Cristofolini L, Schileo E, Juszczuk M, Taddei F, Martelli S, Viceconti M. 2010. Mechanical testing of bones: the positive synergy of finite-element models and *in vitro* experiments. *Philos Trans A Math Phys Eng Sci.* 368:2725–2763.
- Cristofolini L, Viceconti M. 1997. Comparison of uniaxial and triaxial rosette gages for strain measurement in the femur. *Exp Mech.* 37:350–354.
- Cyganik L, Binkowski M, Kokot G, Rusin T, Popik P, Bolechała F, Nowak R, Wróbel Z, John A. 2014. Prediction of Young's modulus of trabeculae in microscale using macro-scale's relationships between bone density and mechanical properties. *J Mech Behav Biomed Mater.* 36:120–134.
- Dall'Ara E, Barber D, Viceconti M. 2014. About the inevitable compromise between spatial resolution and accuracy of strain measurement for bone tissue: a 3D zero-strain study. *J Biomech.* 47:2956–2963.
- Dickinson AS, Taylor AC, Browne M. 2012. The influence of acetabular cup material on pelvis cortex surface strains, measured using digital image correlation. *J Biomech.* 45:719–723.
- Dickinson AS, Taylor AC, Ozturk H, Browne M. 2011. Experimental validation of a finite element model of the proximal femur using digital image correlation and a composite bone model. *J Biomech Eng.* 133:014504.
- Estrada JB, Franck C. 2015. Intuitive interface for the quantitative evaluation of speckle patterns for use in digital image and volume correlation techniques. *J Appl Mech.* 82:095001.
- Evans SL, Holt CA. 2009. Measuring the mechanical properties of human skin *in vivo* using digital image correlation and finite element modelling. *J Strain Anal Eng Des.* 44:337–345.
- Freddi A, Olmi G, Cristofolini L. 2015. Experimental stress analysis for materials and structures: stress analysis models for developing design methodologies. Cham: Springer.
- Gao Z, Desai JP. 2010. Estimating zero-strain states of very soft tissue under gravity loading using digital image correlation. *Med Image Anal.* 14:126–137.

- Gao J, Xu W, Geng J. 2006. 3D shape reconstruction of teeth by shadow speckle correlation method. *Opt Lasers Eng.* 44:455–465.
- Genovese K, Casaletto L, Humphrey JD, Lu J. 2014. Digital image correlation-based point-wise inverse characterization of heterogeneous material properties of gallbladder *in vitro*. *Proc R Soc A Math Phys Eng Sci.* 470:20140152–20140152.
- Genovese K, Casaletto L, Rayas JA, Flores VMA. 2013. Stereodigital image correlation (DIC) measurements with a single camera using a biprism. *Opt Lasers Eng.* 51:278–285.
- Genovese K, Collins MJ, Lee YU, Humphrey JD. 2012. Regional finite strains in an angiotensin-II induced mouse model of dissecting abdominal aortic aneurysms. *Cardiovasc Eng Technol.* 3:194–202.
- Genovese K, Humphrey JD. 2015. Multimodal optical measurement *in vitro* of surface deformations and wall thickness of the pressurized aortic arch. *J Biomed Opt.* 20:046005.
- Genovese K, Lee YU, Humphrey JD. 2011. Novel optical system for *in vitro* quantification of full surface strain fields in small arteries: II. Correction for refraction and illustrative results. *Comput Methods Biomech Biomed Eng.* 14:227–237.
- Genovese K, Lee Y-U, Lee AY, Humphrey JD. 2013. An improved panoramic digital image correlation method for vascular strain analysis and material characterization. *J Mech Behav Biomed Mater.* 27:132–142.
- Genovese K, Montes A, Martínez A, Evans SL. 2015. Full-surface deformation measurement of anisotropic tissues under indentation. *Med Eng Phys.* 37:484–493.
- Ghosh R, Gupta S, Dickinson A, Browne M. 2012. Verification of the digital image correlation technique for bone surface strain measurements. *J Biomech.* 45:S277.
- Gilchrist S, Guy P, Crompton PA. 2013. Development of an inertia-driven model of sideways fall for detailed study of femur fracture mechanics. *J Biomech Eng.* 135:121001.
- Gillard F, Boardman R, Mavrogordato M, Hollis D, Sinclair I, Pierron F, Browne M. 2014. The application of digital volume correlation (DVC) to study the microstructural behaviour of trabecular bone during compression. *J Mech Behav Biomed Mater.* 29:480–499.
- Grassi L, Isaksson H. 2015. Extracting accurate strain measurements in bone mechanics: a critical review of current methods. *J Mech Behav Biomed Mater.* 50:43–54.
- Grassi L, Väänänen SP, Amin Yavari S, Weinans H, Jurvelin JS, Zadpoor AA, Isaksson H. 2013. Experimental validation of finite element model for proximal composite femur using optical measurements. *J Mech Behav Biomed Mater.* 21:86–94.
- Grassi L, Vaananen SP, Yavari SA, Jurvelin JS, Weinans H, Ristinmaa M, Zadpoor AA, Isaksson H. 2014. Full-field strain measurement during mechanical testing of the human femur at physiologically relevant strain rates. *J Biomech Eng.* 136. doi: '10.1115/1.4028415
- Haddadi H, Belhabib S. 2008. Use of rigid-body motion for the investigation and estimation of the measurement errors related to digital image correlation technique. *Opt Lasers Eng.* 46:185–196.
- Han Y, Kim DW, Kwon HJ. 2012. Application of digital image cross-correlation and smoothing function to the diagnosis of breast cancer. *J Mech Behav Biomed Mater.* 14:7–18.
- Helgason B, Gilchrist S, Ariza O, Chak JD, Zheng G, Widmer RP, Ferguson SJ, Guy P, Crompton PA. 2014. Development of a balanced experimental–computational approach to understanding the mechanics of proximal femur fractures. *Med Eng Phys.* 36:793–799.
- Helm JD, McNeill SR, Sutton MA. 1996. Improved three-dimensional image correlation for surface displacement measurement. *Opt Eng.* 35:1911–1920.
- Hild F, Roux S. 2006. Digital image correlation: from displacement measurement to identification of elastic properties – a review. *Strain.* 42:69–80.
- Hoc T, Henry L, Verdier M, Aubry D, Sedel L, Meunier A. 2006. Effect of microstructure on the mechanical properties of Haversian cortical bone. *Bone.* 38:466–474.
- Hokka M, Mirow N, Nagel H, Irsusi M, Vogt S, Kuokkala VT. 2015. *In-vivo* deformation measurements of the human heart by 3D digital image correlation. *J Biomech.* 48:2217–2220.
- Holzappel GA. 2006. Determination of material models for arterial walls from uniaxial extension tests and histological structure. *J Theor Biol.* 238:290–302.
- Hussein AI, Barbone PE, Morgan EF. 2012. Digital volume correlation for study of the mechanics of whole bones. *Procedia IUTAM.* 4:116–125.
- Hussein AI, Mason ZD, Morgan EF. 2013. Presence of intervertebral discs alters observed stiffness and failure mechanisms in the vertebra. *J Biomech.* 46:1683–1688.
- Jones AC, Wilcox RK. 2008. Finite element analysis of the spine: towards a framework of verification, validation and sensitivity analysis. *Med Eng Phys.* 30:1287–1304.
- Jungmann R, Szabo ME, Schitter G, Tang RY, Vashishth D, Hansma PK, Thurner PJ. 2011. Local strain and damage mapping in single trabeculae during three-point bending tests. *J Mech Behav Biomed Mater.* 4:523–534.
- Juszczak MM, Cristofolini L, Viceconti M. 2011. The human proximal femur behaves linearly elastic up to failure under physiological loading conditions. *J Biomech.* 44:2259–2266.
- Karimi A, Navidbakhsh M, Haghghatnama M, Haghi AM. 2015. Determination of the axial and circumferential mechanical properties of the skin tissue using experimental testing and constitutive modeling. *Comput Methods Biomech Biomed Eng.* 18:1768–1774.
- Keaveny PP, Tania RP, Crawford L, David K, Albert L. 1997. Systematic and random errors in compression testing of trabecular bone. *J Orthop Res.* 15:101–110.
- Kelleher JE, Zhang K, Siegmund T, Chan RW. 2010. Spatially varying properties of the vocal ligament contribute to its eigenfrequency response. *J Mech Behav Biomed Mater.* 3:600–609.
- Kelley CT. 1999. Iterative methods for optimization. Raleigh, NC: Society for Industrial and Applied Mathematics.
- Kelly TA, Ng KW, Wang CC, Ateshian GA, Hung CT. 2006. Spatial and temporal development of chondrocyte-seeded agarose constructs in free-swelling and dynamically loaded cultures. *J Biomech.* 39:1489–1497.
- Kim JH, Badel P, Duprey A, Favre JP, Avril S. 2011. Characterisation of failure in human aortic tissue using digital image correlation. *Comput Methods Biomech Biomed Eng.* 14(Suppl1):73–74.
- Larrabee WJ. 1986. A finite element model of skin deformation. I. Biomechanics of skin and soft tissue: a review. *Laryngoscope.* 96:399–405.
- Lava P, Cooreman S, Coppieters S, De Strycker M, Debruyne D. 2009. Assessment of measuring errors in DIC using deformation fields generated by plastic FEA. *Opt Lasers Eng.* 47:747–753.

- Lava P, Cooreman S, Debruyne D. 2010. Study of systematic errors in strain fields obtained via DIC using heterogeneous deformation generated by plastic FEA. *Opt Lasers Eng.* 48:457–468.
- Lava P, Coppieters S, Wang Y, Van Houtte P, Debruyne D. 2011. Error estimation in measuring strain fields with DIC on planar sheet metal specimens with a non-perpendicular camera alignment. *Opt Lasers Eng.* 49:57–65.
- Lecompte D, Bossuyt S, Cooreman S, Sol H, Vantomme J. 2007. Study and generation of optimal speckle patterns for DIC. SEM annual conference & exposition on Experimental and Applied Mechanics. Springfield, MA.
- Lecompte D, Smits A, Bossuyt S, Sol H, Vantomme J, Van Hemelrijck D, Habraken AM. 2006. Quality assessment of speckle patterns for digital image correlation. *Opt Lasers Eng.* 44:1132–1145.
- Li J, Fok AS, Satterthwaite J, Watts DC. 2009. Measurement of the full-field polymerization shrinkage and depth of cure of dental composites using digital image correlation. *Dent Mater.* 25:582–588.
- Libertiaux V, Pascon F, Cescotto S. 2011. Experimental verification of brain tissue incompressibility using digital image correlation. *J Mech Behav Biomed Mater.* 4:1177–1185.
- Lionello G, Cristofolini L. 2014. A practical approach to optimizing the preparation of speckle patterns for digital-image correlation. *Meas Sci Technol.* 25:107001.
- Lionello G, Sirieix C, Baleani M. 2014. An effective procedure to create a speckle pattern on biological soft tissue for digital image correlation measurements. *J Mech Behav Biomed Mater.* 39:1–8.
- Little EG, Tocher D, O'Donnell P. 1990. Strain gauge reinforcement of plastics. *Strain.* 26:91–98.
- Liu L, Morgan EF. 2007. Accuracy and precision of digital volume correlation in quantifying displacements and strains in trabecular bone. *J Biomech.* 40:3516–3520.
- Luo PF, Chao YJ, Sutton MA. 1994. Application of stereo vision to three-dimensional deformation analyses in fracture experiments. *Opt Eng.* 33:981–990.
- Luo PF, Chao YJ, Sutton MA, Peters WH. 1992. Accurate measurement of three-dimensional deformations in deformable and rigid bodies using computer vision. *Exp Mech June:* 123–132.
- Luyckx T, Verstraete M, De Roo K, De Waele W, Bellemans J, Victor J. 2014. Digital image correlation as tool for 3D strain analysis in human tendon tissue. *J Exp Orthop.* 1:7.
- Madi K, Tozzi G, Zhang QH, Tong J, Cossey A, Au A, Hollis D, Hild F. 2013. Computation of full-field displacements in a scaffold implant using digital volume correlation and finite element analysis. *Med Eng Phys.* 35:1298–1312.
- Mann KA, Miller MA, Cleary RJ, Janssen D, Verdonshot N. 2008. Experimental micromechanics of the cement–bone interface. *J Orthop Res.* 26:872–879.
- Marino Cugno Garrano A, La Rosa G, Zhang D, Niu LN, Tay FR, Majd H, Arola D. 2012. On the mechanical behavior of scales from *Cyprinus carpio*. *J Mech Behav Biomed Mater.* 7:17–29.
- McKinley TO, Bay BK. 2003. Trabecular bone strain changes associated with subchondral stiffening of the proximal tibia. *J Biomech.* 36:155–163.
- Moerman KM, Holt CA, Evans SL, Simms CK. 2009. Digital image correlation and finite element modelling as a method to determine mechanical properties of human soft tissue *in vivo*. *J Biomech.* 42:1150–1153.
- Myers KM, Coudrillier B, Boyce BL, Nguyen TD. 2010. The inflation response of the posterior bovine sclera. *Acta Biomater.* 6:4327–4335.
- Myers KM, Paskaleva AP, House M, Socrate S. 2008. Mechanical and biochemical properties of human cervical tissue. *Acta Biomater.* 4:104–116.
- Nagarkatti DG, McKeon BP, Donahue BS, Fulkerson JP. 2001. Mechanical evaluation of a soft tissue interference screw in free tendon anterior cruciate ligament graft fixation. *Am J Sport Med.* 29:67–71.
- Narmoneva DA. 2002. Direct measurement of the Poisson's ratio of human patella cartilage in tension. *J Biomech Eng.* 124:223.
- Nicolella DP, Bonewald LF, Moravits DE, Lankford J. 2005. Measurement of microstructural strain in cortical bone. *Eur J Morphol.* 42:23–29.
- Nicolella DP, Moravits DE, Gale AM, Bonewald LF, Lankford J. 2006. Osteocyte lacunae tissue strain in cortical bone. *J Biomech.* 39:1735–1743.
- Nicolella DP, Nicholls AE, Lankford J, Davy DT. 2001. Machine vision photogrammetry: a technique for measurement of microstructural strain in cortical bone. *J Biomech.* 34:135–139.
- Ning J, Xu S, Wang Y, Lessner SM, Sutton MA, Anderson K, Bischoff JE. 2010. Deformation measurements and material property estimation of mouse carotid artery using a microstructure-based constitutive model. *J Biomech Eng.* 132:121010.
- Okotie G, Duenwald-Kuehl S, Kobayashi H, Wu MJ, Vanderby R. 2012. Tendon strain measurements with dynamic ultrasound images: evaluation of digital image correlation. *J Biomech Eng.* 134:024504.
- Op Den Buijs J, Dragomir-Daescu D. 2011. Validated finite element models of the proximal femur using two-dimensional projected geometry and bone density. *Comput Methods Programs Biomed.* 104:168–174.
- Ottenio M, Tran D, Ní Annaidh A, Gilchrist MD, Bruyère K. 2015. Strain rate and anisotropy effects on the tensile failure characteristics of human skin. *J Mech Behav Biomed Mater.* 41:241–250.
- Palanca M, Brugo TM, Cristofolini L. 2015. Use of digital image correlation to understand the biomechanics of the vertebra. *J Mech Med Biol.* 15:1540001–1540010.
- Palanca M, Tozzi G, Cristofolini L, Viceconti M, Dall'Ara E. 2015. 3D Local Measurements of Bone Strain and Displacement: Comparison of Three Digital Volume Correlation Approaches. *J Biomech Eng (ASME).* 137:071001–071014.
- Pan B, Qian K, Xie H, Asundi A. 2009. Two-dimensional digital image correlation for in-plane displacement and strain measurement: a review. *Meas Sci Technol.* 20:062001.
- Pan B, Xie HM, Wang Z, Qian KM. 2008. Study on subset size selection in digital image correlation for speckle patterns. *Opt Express.* 16:7037–7048.
- Pan B, Yu L, Wu D. 2013. High-accuracy 2D digital image correlation measurements with bilateral telecentric lenses: error analysis and experimental verification. *Exp Mech.* 53:1719–1733.
- Panjabi MM. 2007. Hybrid multidirectional test method to evaluate spinal adjacent-level effects. *Clin Biomech.* 22:257–265.
- Patterson EA, Hack E, Brailly P, Burguete RL, Saleem Q, Siebert T, Tomlinson RA, Whelan MP. 2007. Calibration and evaluation

- of optical systems for full-field strain measurement. *Opt Lasers Eng.* 45:550–564.
- Peters WH, Ranson WF. 1982. Digital imaging techniques in experimental stress analysis. *Opt Eng.* 21:427–431.
- Post D, Han B. 2008. Moiré interferometry. *Handbook on experimental mechanics*. New York: Springer.
- Pyne JD, Genovese K, Casaletto L, Vande Geest JP. 2014. Sequential-digital image correlation for mapping human posterior sclera and optic nerve head deformation. *J Biomech Eng.* 136:021002.
- Roberts BC, Perilli E, Reynolds KJ. 2014. Application of the digital volume correlation technique for the measurement of displacement and strain fields in bone: a literature review. *J Biomech.* 47:923–934.
- Sachs C, Fabritius H, Raabe D. 2006. Experimental investigation of the elastic-plastic deformation of mineralized lobster cuticle by digital image correlation. *J Struct Biol.* 155:409–425.
- Schileo E, Taddei F, Cristofolini L, Viceconti M. 2008. Subject-specific finite element models implementing a maximum principal strain criterion are able to estimate failure risk and fracture location on human femurs tested *in vitro*. *J Biomech.* 41:356–367.
- Schmidt T, Tyson J, Galanulis K. 2003. Full-field dynamic displacement and strain measurement using advanced 3D image correlation photogrammetry: part I. *Exp Tech.* 27:47–50.
- Sebastian C, Patterson EA. 2012. Calibration of a digital image correlation system. *Exp Tech.* 39:21–29.
- Shin TJ, Vito RP, Johnson LW, McCarey BE. 1997. The distribution of strain in the human cornea. *J Biomech.* 30:497–503.
- Smith TS, Bay BK, Rashid F. 2002. Digital volume correlation including rotational degrees of freedom during minimization. *Exp Mech.* 42:272–278.
- Soons J, Lava P, Debruyne D, Dirckx J. 2012. Full-field optical deformation measurement in biomechanics: digital speckle pattern interferometry and 3D digital image correlation applied to bird beaks. *J Mech Behav Biomed Mater.* 14:186–191.
- Spencer M, Siegmund T, Mongeau L. 2008. Determination of superior surface strains and stresses, and vocal fold contact pressure in a synthetic larynx model using digital image correlation. *J Acoust Soc Am.* 123:1089–1103.
- Spera D, Genovese K, Voloshin A. 2011. Application of stereo-digital image correlation to full-field 3-D deformation measurement of intervertebral disc. *Strain.* 47:e572–e587.
- Sutton MA, Ke X, Lessner SM, Goldbach M, Yost M, Zhao F, Schreier HW. 2008. Strain field measurements on mouse carotid arteries using microscopic three-dimensional digital image correlation. *J Biomed Mater Res A.* 84A:178–190.
- Sutton MA, Orteu JJ, Schreier HW. 2009. *Image correlation for shape, motion and deformation measurements*. New York: Springer Science.
- Sutton MA, Wolters WJ, Peters WH, Ranson WF, McNeill SR. 1983. Determination of displacements using an improved digital correlation method. *Image Vision Comput.* 1:133–139.
- Sutton MA, Yan JH, Tiwari V, Schreier HW, Orteu JJ. 2008. The effect of out-of-plane motion on 2D and 3D digital image correlation measurements. *Opt Lasers Eng.* 46:746–757.
- Szefek P, Vanleene M, Olsson R, Collinson R, Pitsillides AA, Sheffellbine S. 2010. Using digital image correlation to determine bone surface strains during loading and after adaptation of the mouse tibia. *J Biomech.* 43:599–605.
- Tan T, Davis FM, Gruber DD, Massengill JC, Robertson JL, De Vita R. 2015. Histo-mechanical properties of the swine cardinal and uterosacral ligaments. *J Mech Behav Biomed Mater.* 42:129–137.
- Tanasic I, Milic-Lemic A, Tihacek-Sojic L, Stancic I, Mitrovic N. 2012. Analysis of the compressive strain below the removable and fixed prosthesis in the posterior mandible using a digital image correlation method. *Biomech Model Mechanobiol.* 11:751–758.
- Tang T, Ebacher V, Crompton P, Guy P, McKay H, Wang R. 2015. Shear deformation and fracture of human cortical bone. *Bone.* 71:25–35.
- Tayton E, Evans S, O'Doherty D. 2010. Mapping the strain distribution on the proximal femur with titanium and flexible-stemmed implants using digital image correlation. *J Bone Joint Surg.* 92-B:1176–1181
- Thompson ML, Backman D, Branemark R, Mechefske CK. 2011. Evaluating the bending response of two osseointegrated transfemoral implant systems using 3D digital image correlation. *J Biomech Eng.* 133:051006.
- Thompson MS, Schell H, Lienau J, Duda GN. 2007. Digital image correlation: a technique for determining local mechanical conditions within early bone callus. *Med Eng Phys.* 29:820–823.
- Tiossi R, Lin L, Conrad HJ, Rodrigues RC, Heo YC, de Mattos Mda G, Fok AS, Ribeiro RF. 2012. A digital image correlation analysis on the influence of crown material in implant-supported prostheses on bone strain distribution. *J Prosthodont Res.* 56:25–31.
- Tiossi R, Lin L, Rodrigues RC, Heo YC, Conrad HJ, de Mattos Mda G, Ribeiro RF, Fok AS. 2011. Digital image correlation analysis of the load transfer by implant-supported restorations. *J Biomech.* 44:1008–1013.
- Tozzi G, Zhang QH, Tong J. 2014. Microdamage assessment of bone–cement interfaces under monotonic and cyclic compression. *J Biomech.* 47:3466–3474.
- Tyson J, Schmidt T, Galanulis K. 2002. Biomechanics deformation and strain measurements with 3D image correlation photogrammetry. *Exp Tech.* 26:39–42.
- Vaananen SP, Amin Yavari S, Weinans H, Zadpoor AA, Jurvelin JS, Isaksson H. 2013. Repeatability of digital image correlation for measurement of surface strains in composite long bones. *J Biomech.* 46:1928–1932.
- Wahba G. 1975. Smoothing noisy data with spline functions. *Numer Math.* 24:383–393.
- Wang CCB, Chahine NO, Hung CT, Ateshian GA. 2003. Optical determination of anisotropic material properties of bovine articular cartilage in compression. *J Biomech.* 36:339–353.
- Wang CCB, Deng J-M, Ateshian GA, Hung CT. 2002. An automated approach for direct measurement of two-dimensional strain distributions within articular cartilage under unconfined compression. *J Biomech Eng.* 124:557.
- Wang Y, Lava P, Coppieters S, De Strycker M, Van Houtte P, Debruyne D. 2012. Investigation of the uncertainty of DIC under heterogeneous strain states with numerical tests. *Strain.* 48:453–462.
- Weisbecker H, Pierce DM, Regitnig P, Holzapfel GA. 2012. Layer-specific damage experiments and modeling of human thoracic and abdominal aortas with non-atherosclerotic intimal thickening. *J Mech Behav Biomed Mater.* 12:93–106.
- Woltring HJ. 1985. On optimal smoothing and derivative estimation from noisy displacement data in biomechanics. *Hum Movement Sci.* 4:229–245.

- Yamaguchi H, Kikugawa H, Asaka T, Kasuya H, Kuninori M. 2011. Measurement of cortical bone strain distribution by image correlation techniques and from fracture toughness. *Mater Trans.* 52:1026–1032.
- Yang PF, Bruggemann GP, Ritteweger J. 2011. What do we currently know from *in vivo* bone strain measurements in humans? *J Musculoskelet Neuron Interact.* 11:8–20.
- Yaofeng S, Pang JHL. 2007. Study of optimal subset size in digital image correlation of speckle pattern images. *Opt Lasers Eng.* 45:967–974.
- Yoneyama S. 2006. Lens distortion correction for digital image correlation by measuring rigid body displacement. *Opt Eng.* 45:023602.
- Zani L, Erani P, Grassi L, Taddei F, Cristofolini L. 2015. Strain distribution in the proximal Human femur during *in vitro* simulated sideways fall. *J Biomech.* 48:2130–2143.
- Zhang D, Arola DD, Eggleton C. 2002a. Measurement of Poisson's ratio of bovine aorta using digital image correlation. *Proc Inst Second Joint EMBS.* 2: 1276–1277.
- Zhang D, Eggleton CD, and Arola D. D.. 2002b. Evaluating the mechanical behavior of arterial tissue using digital image correlation. *Exp Mech.* 42:409–416.
- Zhang D, Arola DD. 2004. Applications of digital image correlation to biological tissues. *J Biomed Opt.* 9:691–699.
- Zhang J, Jin GC, Meng LB, Jian LH, Wang AY, Lu SB. 2005. Strain and mechanical behavior measurements of soft tissues with digital speckle method. *J Biomed Opt.* 10:034021.
- Zhang D, Nazari A, Soappman M, Bajaj D, Arola D. 2007. Methods for examining the fatigue and fracture behavior of hard tissues. *Exp Mech.* 47:325–336.

Appendix 1.

DIC uses digital images to track the displacement of portions of the speckled surface (Figure 1). In the case of 2D-DIC, images of specimen surface in the undeformed (or reference) and deformed states are acquired by one high-spatial-resolution digital image acquisition device (such as a regular digital camera, a high-speed camera, an optical microscope). The digital images (typically in grey scale) are divided into sub-images (facets). In order to obtain an approximation of grey scale between pixels instead of discrete and independent values, the grey-scale distributions are interpolated, usually with a bicubic spline. Images of the deformed states are compared to the reference one in order to match facets and track the displacement. The degree of matching between facets is evaluated by a normalized cross-correlation function such as (A1):

$$\rho_{CC} = \frac{\sum_{i=1}^N \sum_{j=1}^M F(x_i, y_j) G(x'_i, y'_j)}{\sqrt{\sum_{i=1}^N \sum_{j=1}^M F^2(x_i, y_j) \sum_{i=1}^N \sum_{j=1}^M G^2(x'_i, y'_j)}} \quad (\text{A1})$$

or a normalized sum-of-squared-differences such as (A2):

$$\rho_{SSD} = \sum_{i=1}^N \sum_{j=1}^M \left[\frac{F(x_i, y_j)}{\sqrt{\sum_{i=1}^N \sum_{j=1}^M F^2(x_i, y_j)}} - \frac{G(x'_i, y'_j)}{\sqrt{\sum_{i=1}^N \sum_{j=1}^M G^2(x'_i, y'_j)}} \right]^2 \quad (\text{A2})$$

where $F(x, y)$ and $G(x', y')$ represent the grey-scale value for the pixel at the coordinate (x, y) of the reference image and the coordinate (x', y') of the deformed image, respectively. N and M are the dimensions of the facet, usually square. After matching the facets, the full-field displacement is automatically computed by tracking the change in position of points on digitized images. In fact, the coordinates in the reference image (x, y) and in the deformed one (x', y') describe the deformation between the two states (A3):

$$\begin{aligned} x' &= x + u + \frac{\partial u}{\partial x} \Delta x + \frac{\partial u}{\partial y} \Delta y \\ y' &= y + v + \frac{\partial v}{\partial x} \Delta x + \frac{\partial v}{\partial y} \Delta y \end{aligned} \quad (\text{A3})$$

where u and v represent the displacements for the facet centres in the x and y directions, respectively. Δx and Δy are the distances in the x and y directions, from the centres of the facet to the point in coordinates (x, y) . The gradient terms in A3 indicate that the initial facet of $(M \times N)$ pixels will be strained to optimally match the correspondent facet in the deformed status (Peters & Ranson 1982; Bruck et al. 1989; Wang et al. 2002).

The strain tensor (A4) is obtained by derivation on displacement gradients (Sutton et al. 2009):

$$\begin{aligned} e_{xx} &= \frac{\partial u}{\partial x} + \frac{1}{2} \left[\left(\frac{\partial u}{\partial x} \right)^2 + \left(\frac{\partial v}{\partial x} \right)^2 \right] \\ e_{yy} &= \frac{\partial v}{\partial y} + \frac{1}{2} \left[\left(\frac{\partial u}{\partial y} \right)^2 + \left(\frac{\partial v}{\partial y} \right)^2 \right] \\ e_{xy} &= \frac{1}{2} \left(\frac{\partial u}{\partial y} + \frac{\partial v}{\partial x} \right) + \frac{1}{2} \left[\left(\frac{\partial u}{\partial x} \right) \left(\frac{\partial u}{\partial y} \right) + \left(\frac{\partial v}{\partial x} \right) \left(\frac{\partial v}{\partial y} \right) \right] \end{aligned} \quad (\text{A4})$$

In order to find the six deformation parameters $(u, v, \left(\frac{\partial u}{\partial x}\right), \left(\frac{\partial u}{\partial y}\right), \left(\frac{\partial v}{\partial x}\right), \left(\frac{\partial v}{\partial y}\right))$ and match the facet, an approximate-solution method is adopted. Usually, the Newton–Raphson algorithm is used because of its computational economy (Kelley 1999). Other algorithms are also adopted, such as the Levenberg–Marquardt. When the method converges, the displacement field is obtained but discontinuities might appear due to the local grey-scale value. A smoothing algorithm is needed to provide a continuous displacement field and perform a strain analysis. Among the available smoothing algorithms (Wahba 1975; Woltring 1985), some are better suited than others, depending on the features of the noise to be attenuated (Baldoni et al. 2015). 3D-DIC can be considered as an extension of 2D-DIC, as the operating principles are similar, but extended on a third dimension (Luo et al. 1992) by using two or more cameras in stereoscopic vision.